LAWRENCE
LIVERMORE
NATIONAL
LABORATORY

LLNL-JRNL-402939

The Effect of HF/NH4F Etching on the Morphology of Surface Fractures on Fused Silica

L. Wong, T. Suratwala, M. D. Feit, P. E. Miller, R. A. Steele

April 14, 2008

Journal of Non-Crystalline Solids

Disclaimer

The Effect of HF/NH_4F Etching on the Morphology of Surface Fractures on Fused Silica

L. Wong, T. Suratwala, M. D. Feit, P. E. Miller, R. Steele
Lawrence Livermore National Laboratory, P.O. Box 808, Livermore, CA 94551, USA

ABSTRACT

The effects of HF/NH_4F, wet chemical etching on the morphology of individual surface fractures (indentations, scratches) and of an ensemble of surface fractures (ground surfaces) on fused silica glass has been characterized. For the individual surface fractures, a series of static or dynamic (sliding) Vickers and Brinnell indenters were used to create radial, lateral, Hertzian cone and trailing indentation fractures on a set of polished fused silica substrates which were subsequently etched. After short etch times, the visibility of both surface and subsurface cracks is significantly enhanced when observed by optical microscopy. This is attributed to the removal of the polishing-induced Bielby layer and the increased width of the cracks following etching allowing for greater optical scatter at the fracture interface. The removal of material during etching was found to be isotropic except in areas where the etchant has difficulty penetrating or in areas that exhibit significant plastic deformation/densification. Isolated fractures continue to etch, but will never be completely removed since the bottom and top of the crack both etch at the same rate.

The etching behavior of ensembles of closely spaced cracks, such as those produced during grinding, has also been characterized. This was done using a second set of fused silica samples that were ground using either fixed or loose abrasives. The resulting samples were etched and both the etch rate and the morphology of the surfaces were monitored as a function of time. Etching results in the formation of a series of open cracks or cusps, each corresponding to the individual fractures originally on the surface of the substrate. During extended etching, the

individual cusps coalesce with one another, providing a means of reducing the depth of subsurface damage and the peak-to-valley roughness. In addition, the material removal rate of the ground surfaces was found to scale with the surface area of the cracks as a function of etch time. The initial removal rate for the ground surface was typically 3.5× the bulk etch rate. The evolving morphology of ground surfaces during etching was simulated using an isotropic finite difference model. This model illustrates the importance that the initial distributions of fracture sizes and spatial locations have on the evolution of roughness and the rate at which material is removed during the etching process. The etching of ground surfaces can be used during optical fabrication to convert subsurface damage into surface roughness thereby reducing the time required to produce polished surfaces that are free of subsurface damage.

1. INTRODUCTION

Fluoride based wet chemical etching can be accomplished by using a variety of reagents including hydrofluoric acid (HF) or, under suitably acidic conditions, fluoride or bifluoride salts. The dissolution of silicate glasses results in the formation of the stable hexafluorosilicate (SiF_6^{2-}) anion [1-11]. When hydrofluoric acid is used, the overall reaction can be summarized as:

$$SiO_2 + 6\ HF \rightarrow SiF_6^{2-} + 2\ H_2O + 2\ H^+ \quad (1)$$

The underlying mechanism of such reactions involves a number of steps and intermediate species. For example, in aqueous solution, HF acid acts as a weak acid where an equilibrium exists between the un-dissociated acid, H^+ ions and the F^- anions:

$$HF \rightarrow H^+ + F^- \qquad {}^{25}K_a = 6.7\times10^{-4}\ mol/l \quad (2)$$

where ${}^{25}K_a$ is the equilibrium constant at 25°C [12] .

In the presence of un-dissociated HF, the fluoride ion reacts to form the bifluoride anion (HF_2^-) which is thought to be a primary species responsible for the attack of the silica matrix [2,11,12]:

$$HF + F^- \rightarrow HF_2^- \qquad {}^{25}K = 3.96\ mol/l \quad (3)$$

A variety of reagents, so long as they produce both fluoride (F^-) and hydrogen (H^+) ions, can form the bifluoride ions in-situ, and thus can be expected to etch silicate glasses.

In the present study, solutions of buffered oxide etch (BOE) were used as the etchant. However, qualitatively similar results would be expected using other fluoride based etchants. BOE refers to a series of commercially available mixtures of high purity, aqueous-phase hydrofluoric acid (HF) and ammonium fluoride (NH_4F) which were developed for use in the semiconductor industry [1, 2, 9, 10]. In such solutions, NH_4F dissociates completely providing

an abundant source of F^- ions which are free to react with the un-dissociated HF to form HF_2^- ions (Eq. 3). In addition, the small fraction of dissociated HF (Eq. 2) provides the H^+ ions which are known to catalyze the overall reaction [13].

Most contemporary studies of fluoride etching on glass surfaces have been performed in the context of the semiconductor industry. Such studies most often concentrate on masking and dielectric film applications, and describe the evolution of masked silica surfaces with etch time [1,2,14,15]. Significantly less work has been reported on the use of fluoride etching during optical fabrication. Preston [3] was among the first to examine how HF etching on ground surfaces of glass changes the surface topology of glass and recognized the utility of acid etching as an inspection aid. Spierings [1] combined the results from the glass science and integrated circuit (IC) fabrication literature in a comprehensive review that describes the etching mechanism, morphological changes of glass surfaces with etching, and the effects of etchant and glass composition [1]. More recently, Zhou et al. [4] and the present authors [5-7], applied HF etching to reveal subsurface cracks.

In the present work, we report on the effect that fluoride etching has on the morphology and observability of three classes of fractures: static indentation fractures (digs), sliding indentation fractures (scratches), and ensembles of fractures typical of ground fused silica surfaces. The present work suggests the use of etching both as an aid in the inspection process and as a means of removing subsurface fractures/damage (SSD) introduced during the fabrication and finishing of silicate based glasses or ceramics, particularly in those applications where SSD must be minimized in the final product. Examples include the finishing of SSD free optics for use in high-peak-power laser systems [16] and applications where material strength is

of paramount importance, such as for windows or barriers used in aerospace or deep-sea applications.

2. EXPERIMENTAL PROCEDURES

2.1 Etching of Isolated Fractures (Static and Sliding Indentations)

A series of static and sliding indentations were created, under ambient conditions, on the surface of polished fused silica (Corning 7980) substrates and the morphology of these cracks was monitored as a function of BOE etch time. Static Hertzian (blunt) fractures were created on a polished, fused silica substrate (Corning 7980; $7 \times 7 \times 0.7$ cm^3) using a 1 mm diameter stainless steel Brinnell indenter using a Zwick microhardness tester (Model 3212) using loads of 39 N and 49 N. A loading rate of 0.3 mm/sec and a dwell time of 60 seconds were used in each case. Static Vickers (sharp) indentations were also created on the same substrate using a standard Vickers diamond indenter at loads of 1, 2, 59, 78 and 98 N. The 1 N and 2 N loads were applied using a Shimadzu microhardness tester (Model HMV2) while the 59, 78 and 98 N loads were applied using the Zwick microhardness tester. In all cases, the loading rate was nominally 0.2 mm/sec and the dwell time was 60 seconds. Finally, a series of sliding blunt indentations [5,17]) were created by sliding an 11 mm diameter stainless steel ball across the substrate surface at ~1 cm/sec with a nominal load of ~90 N.

All etching was performed by affixing the substrate to a Teflon® kinematic mount. The entire assembly was then immersed in 20:1 BOE (Air Products, Allentown, PA) for various etch times and subsequently removed from the etchant for characterization. This characterization included weighing of the sample to the nearest 1 mg, recording the surface morphology, in both reflection and transmission using optical microscopy (Nikon Optiphot 300), and recording

surface topology using a stylus profilometer (KLA Tencor P-10). The kinematic mount provided a means of reproducibly mounting the sample during subsequent characterization and metrology cycles so that the same location of the substrate could be measured and characterized.

2.2 Etching of Ground Surfaces

One of the faces of each round fused silica samples (Corning 7980; 10 cm diameter × 1.0 cm thick; polished on all surfaces) was ground using either fixed or loose abrasive processes. The first sample was ground using a Model II Blanchard (S/N 7769) equipped with a 150 grit (100 μm) diamond in a metal matrix tool (downward feed rate = 230 μm/min, rotation rate = 41 rpm, time= 20 sec). The second sample was loose-abrasive ground on an 8" borosilicate glass lap (load = 0.3 psi, rotation rate = 15 rpm, time = 1 hr) using a 30 μm Al_2O_3 abrasive particle slurry (Microgrit WCA30T). The SSD distributions of the two ground surfaces (150 grit, fine Blanchard and 30 μm, loose abrasive) were determined by: 1) creating a shallow (~40-50 μm) wedge/taper on the surface by magneto-rheological finishing (MRF); 2) exposing the SSD by acid etching; and 3) performing image analysis of the observed cracks from optical micrographs taken along the surface taper. Details of this characterization technique are provided elsewhere [5-7]. A second set of the ground samples described above were etched for various times in 20:1 BOE and characterized in the same manner as described in Section 2.1.

3. RESULTS

3.1 Etching of Static and Sliding Indentations

Figure 1 shows optical micrographs and the surface profilometry of the static Brinnell and Vickers indentations before etching and as each indentation fracture evolved during a total of

18 hours of etching. The morphology of the surface before etching was typical of those expected following Brinnell (Hertizan cone cracks) and Vickers (radial and lateral cracks) indentation (see Fig. 2 and top of Fig. 1). In the absence of etching, the surface ring crack at 39 N is barely visible (Fig. 1a). At a higher applied load of 49 N, the ring crack is more discernible although the extent of the surface fracture in either case is not readily apparent (Fig. 1b). After even a short etch time (30 minutes), corresponding to the removal of ~500 nm of material, both the surface cracks and the overall depth and extent of the subsurface fractures resulting from each indentation are much more apparent. It should also be noted that even after long etch times (18 hours), each of the isolated fractures are clearly discernible. This is a result of the isotropic nature of the etching process where the bottom of the crack etches at nominally the same rate as the sides of the crack.

Figures 1c and 1d show the Vickers indentations at 1 N and 2 N, respectively. Prior to etching, the presence of radial and lateral cracks, as well as a plastically deformed or densified zone, are discernible. Following etching, however, in addition to the expected radial and lateral cracks, Hertzian (cone) [17] cracks are also present in each case. This was similarly observed for the Vickers indentations created at the higher loads (Fig. 3). The anomalous presence of such cone cracks, induced by a sharp indenter in fused silica, has previously been described by Roesler [18] and Hagan [19].

Finally, Fig. 4 shows the morphological changes of a series of trailing indentation cracks (i.e. a scratch) as a function of etch time. At short etch times, the individual fractures remained isolated from one another. At longer etch times, these cracks etch open to form cusps which can be described as rounded pits on the surface having depths equivalent to the crack depth. With sufficient etching, the cusps, corresponding to each of the individual cracks, coalesce with one

another to form a nearly continuous trench on the surface of the optic. However, because this coalescence occurs only along a single dimension, along the surface of the optic, the scratch remains prominent even after 120 hours of etching.

3.2 Etching of Ground Surfaces

Figure 5 shows a series of optical micrographs and the surface profilometry scans that were taken at approximately the same location after various etch times for the two ground fused silica surfaces. Figure 5a describes the results for the etched fused silica substrate which was ground using the 150 grit fixed abrasive, while Fig. 5b describes the results for the sample which was ground using the 30 μm loose abrasive. Etching results in the formation of a series of individual cusps which are created as silica is etched from the sides and bottom of each fracture site. As etching progresses, individual cusps coalesce with one another resulting in the formation of successively larger cusps. As shown in Fig. 6, one finds that the average cusp diameter scales with the square root of time. Unlike a scratch, ground surfaces consist of an ensemble of closely spaced fractures that are randomly distributed on the surface. As material is etched from the sides of individual fractures, individual cusps intersect and coalesce with one another. Such coalescence increases both the spatial period of the surface roughness and removes SSD.

The SSD depth distributions (cumulative crack obscuration, O(c), as a function of depth) for both the fixed and loose abrasive ground samples are shown in Fig. 7. The maximum SSD depth was found to be ~42 μm for the Blanchard-ground sample and ~41 μm for the loose abrasive ground sample (see Table 1).

4. DISCUSSION

4.1 Etching of Isolated Fractures

During the polishing of high quality optical components or high strength glass or ceramic components, it is often desirable to determine the origin of, or the extent of, scratches (sliding indentation) or digs (static indentation), which can occur during fabrication or the handling process. The size and morphology of the indentation cracks combined with a knowledge of the fundamental aspects of tribology [20] and indentation fracture [17] can be utilized as a tool for determining the nature of the indenter (sharp vs. blunt), the physical size of the indenter, and the load which must have been present during the indentation event [5-7]. Such information, when combined with specific process knowledge, can often be used to indentify the process or handling steps during which specific flaws were introduced.

In this context the fluoride etching of fused silica has two benefits: (1) exposing surface cracks (Fig. 8) and (2) revealing the true morphology of the cracks (Figs. 9a-c). For example, a short etch of a glass surface typically reveals all of the hidden subsurface damage (i.e. surface fractures) by two means. First, etching removes the index-matched layer of re-deposited or rehydrated silica (the Bielby layer) which typically covers the first ~100 nm of polished glass surfaces [21]. Secondly, etching increases the size and separation of those fracture surfaces which were too narrow to scatter or reflect light prior to etching (see Figs. 8a and 8b).

The crack morphologies for the Brinnell (Hertzian) indentations, Vickers indentations and trailing Hertzian indentations created in this study are well known and have been previously described [5-7,17,20]. An idealized schematic representation of each crack type is shown in Fig. 9.

Using elastic Hertzian contact mechanics [17], the size of the contact zone (2a) between a spherical indenter and a planar surface is given by:

$$2a = 2\left(\frac{4P\,r\,k}{3E}\right)^{\frac{1}{3}} \tag{4}$$

where P is the applied load, r is the radius of the spherical indenter, E is the Young's modulus of the substrate, and k is the contact parameter which is defined as:

$$k = \frac{9}{16}\left[(1-\nu^2) + \frac{E}{E_p}(1-\nu_p^2)\right] \tag{5}$$

where ν and ν_p are Poisson's ratio for the substrate and the indenter, and E_p is the modulus of the indenter. Substituting known material constants for fused silica (substrate) and stainless steel (indenter) [22], the contact zone sizes (2a) for a Brinnell indentation at 39 N and 49 N are found to be 126 μm and 136 μm, respectively. As shown in Figs. 1a and 1b, these values are in reasonable agreement with the measured size of the surface ring cracks which were found to be 131 μm and 135 μm, respectively.

The profilometry results for the Brinnell indentations revealed that the true depth for these cracks can not be measured using contact profilometry due to the narrow width of crack opening [18-20] relative to the size of the profilometry stylus. In comparing the fracture profiles shown in Figs. 1a and 1b to the predicted etching behavior shown in Fig. 9a, the combination of the narrow width of the cracks, the angle of the cone cracks, the width of the stylus (10 μm), and the angle of the stylus, prevents the stylus from providing a true representation of the crack depth at short etch times. However, the width of the opening of the Hertzian cracks after each etch time could still be accurately measured by profilometry and/or microscopy (Figs. 1a and 1b). By

simple geometry, the width of the fracture opening (w_h) with etch time (t), assuming isotropic etching, is given by:

$$w_h = \frac{2 r_b t}{\sin \theta} \tag{6}$$

where r_b is the bulk etch rate expressed in units of thickness/unit time, and θ is the angle of the crack relative to surface of the glass (see Fig. 10). By measuring the depth of the Hertzian cone crack and the distance away from the contact ring, θ is found to be ≈26°; which is similar to that cited by Hagan [19]. Assuming a bulk etch rate of 1.6 μm/hr, which is typical for 20:1 BOE, one can compare the size of the cone crack determined experimentally to the dimensions of the crack that can be calculated assuming isotropic etching (see Eq. 6). Figure 11a compares the measured value of w_h, from the profilometry results in Figs. 1a and 1b, with that calculated using Eq. 6. The good agreement between the two suggests that etching occurs nearly isotropically for Hertzian cone cracks.

Unlike ideal blunt indentations, which take place under purely elastic conditions, sharp indentations involve irreversible or plastic deformation. In particular, sharp indentations typically result in the formation of radial and lateral cracks, together with a plastically deformed and/or densified zone directly below where the indenter contacts the surface (see Fig. 9b). In contrast to Hertzian cracks, the radial cracks from the Vickers indentations were not found to etch isotropically. This effect is illustrated in Fig. 11b where the half-width of the radial crack $\left(\frac{w_r}{2}\right)$ is plotted versus the etch time. As shown in this figure, the radial cracks were found to etch ~20-25% slower than would be expected assuming an isotropic etch rate. One would assume that the plastic deformation and/or densification associated with the sharp indentation(s) result in the reduced etch rate.

In the absence of fluoride etching, either direct or microscopic examination of indentation fractures can lead one to misinterpret the morphology or extent of a fracture or fracture system. For example, when one compares the apparent size of fractures formed as the result of a Vickers indentation prior to (top of Figs. 1a and 1b) and after etching (middle of Figs. 1c and 1d) one finds that the true extent of damage differs by a factor of approximately ten. This difficulty results from both the presence of an index matched hydrated layer, the so-called Bielby layer [21], which is formed during the polishing process, and the partial healing [23] of indentation fractures that may occur following removal of the tension induced by the indenter. Both of these effects reduce the light reflection at the crack surface, thus making these cracks invisible before etching.

4.2 Etching of Ground Surfaces

4.2.1 Cusp Growth Rates

Etching ground surfaces results in the formation of cusps. As described by Spierings [1], each cusp originates from the etching of an individual surface fracture. As shown in Fig. 6, the cusp diameter (D) scales with the square root of etch time ($t^{1/2}$). Although the mechanisms differ significantly, the formalisms describing the growth rate of such cusps and grain growth in polycrystalline ceramics [24] are similar. Specifically, the diameter of each cusp (D) grows at a rate that is inversely proportional to its size:

$$\frac{dD}{dt} = \frac{k_c}{D} \tag{7}$$

where k_c is a growth constant. Integration of Equation 7 gives:

$$D = \sqrt{2k_c t + D_o^{\,2}} \tag{8}$$

where D_o is the initial cusp or crack size. When $D_o << D$, then $D = \sqrt{2k_c t}$ or $D \propto t^{1/2}$. As shown in Fig. 6, experimental data from both the fixed and loose abrasive grinding processes are consistent with the stated dependence and result in similar growth constants (0.01 μm^2/sec for the 150 grit fixed abrasive sample and 0.006 μm^2/sec for the 30 μm loose abrasive sample). One would expect the cusp growth constant to be a function of crack distribution (depth, length, spacing and orientation) (see Section 4.3).

4.2.2 Material Removal

The number density of cracks on a ground surface is typically so high that cracks overlap each other, obscuring the identification or depth of individual fractures. Previous work [5-7] has shown that as several micrometers of material are polished from a ground surface, one finds that the number density of cracks drops exponentially until a maximum depth of subsurface damage is reached [5-7]. The rate at which material is removed during etching is dependent on the surface area exposed to the etchant. Given this, one would expect the rate of material removal during etching to decrease exponentially as the number of fractures in the near surface region of the substrate decreases.

Consider a disk of radius, r_s, and thickness, h_s, which has been ground on one surface and polished on the opposite face and along the edge. The time dependent mass of material removed during etching (m_t) is the sum of the masses that are removed from both the ground (m_g) portion of the sample and the polished (m_p) surfaces of the disk. Thus, one can express m_g as a function of the bulk etch rate (r_b), the dimensions of the disk (r_s and h_s), the etch time (t), and the density of fused silica (ρ = 2.2 gms/cm^3):

$$m_g = m_t - m_p = m_t - r_b\left(\pi r_s^{\,2} + 2\pi r_s h_s\right)\rho t \tag{9}$$

Similarly, the thickness removed from the ground surface, z_g, is given by:

$$z_g = \frac{m_g}{\pi r_s^2 \rho} \tag{10}$$

where πr_s^2 is the geometric area of the ground surface.

Figure 12 shows the material removal rate ($\Delta z_g/\Delta t$) of the ground faces using Eqs. 9 and 10. The rate at which material is etched from the ground surface drops exponentially and reaches an asymptotic value that is equivalent to the etching rate of the bulk fused silica.

The behavior illustrated in Fig. 12 suggests that the surface area initially available to the etchant on the ground faces is about 3.5 times larger than that of the similarly sized polished face. As the cusps associated with each fracture coalesce with one another during the etch process, the true surface area (e.g the area available to the etchant) diminishes until it becomes equivalent to the nominal geometric surface area at which time the rate at which material is etched from each face of the disk becomes equivalent to the bulk etch rate.

4.2.3 Roughness Evolution

The formation, growth, and coalescence of cusps, which result from the local dissolution of silica in the immediate vicinity of individual fracture sites, implies a change in the roughness of a ground surface as it is etched. As shown in Fig. 5, the surface profiles for the samples ground with the 150-grit fixed abrasive and the 30 μm loose abrasive, respectively, show that the cusp size not only grows with etch time, but the surfaces appear to become smoother as well.

Characterizing the surface roughness in terms of the power spectral density ($PSD(k_z)$) as a function of spatial frequency k_z provides one with a means of examining how the surface roughness evolves as a function of etch time. The function $PSD(k_z)$ was calculated from the Fourier transform of the profilometry data $h_z(x)$ using the expression:

$$PSD(k_z) = \frac{\left| \int_{-\infty}^{\infty} h_z(x) e^{-ik_z x} dx \right|^2}{L} \quad (11)$$

where $h_z(x)$ is the raw profilometry data (height vs. position along surface), L is the length of profilometry scan performed and k_z is the spatial frequency. The spatial frequency range for which the PSD is valid is bound by the length of the scan and the spatial length over which each data point is taken. The bounds of the spatial frequency range which can be represented range between 3/L for the long scale length features and n/8L (i.e. Nyquist number/4) for short scale length features where n is the number of data points in the profilometry scan. For the current data set, n = 10,000 and L = 5000 μm, resulting in a spatial frequency range from 0.0006 – 0.25 μm^{-1}, or spatial periods between 4 – 1700 μm.

The calculated PSD from the measured profilometry data, at various etch times, for both the fixed and loose abrasive ground samples is shown in Fig. 13. The behavior of the PSD for each of the ground surfaces appears to differ for features which have spatial frequencies that are greater than and less than ~0.02 μm^{-1}. For features having spatial frequencies less than 0.02 μm^{-1} (> 50 μm spatial period) the PSD (apparent roughness) appears to increase with etch time and reaches a rough plateau. In contrast, the PSD of features having a spatial frequency greater than about 0.02 μm^{-1} (< 50 μm spatial period) appears to reach a maximum value which then falls during extended etching. These effects are more clearly illustrated in Fig. 14, which shows the peak-to-valley (P-V) roughness and root-mean-square (RMS) roughness calculated for both samples as a function of etch time over the spatial ranges described above. The apparent increase in roughness in each case is simply an artifact due to the increased ability of the finite-sized profilometer stylus to penetrate the surface cracks as they etch open (see Section 4.1). The

subsequent drop in small-scale (<50 μm) roughness is due to the coalescence of intersecting cusps.

4.2.4 Cusp Coalescence

The coalescence of neighboring cusps during etching is of central importance in understanding the changes in etch rate, surface roughness and SSD that occur during the etching process. A simple geometric model can be used to describe the key features of cusp coalescence and to provide an understanding of how the surface topography would be expected to evolve as a function of etch time.

For the present, let us assume that the surface consists of an infinite series of equally spaced cracks of uniform depth (c), separated by a distance (s) (see Fig. 15). Fractures on real surfaces, of course, are characterized by a distribution of crack depths and spacings. A refined model reflecting this will be described in Section 4.3 and in the Appendix.

As shown in Fig. 15, at t = 0, etching has not yet started and each crack remains closed. At time t_1, the cracks begin to etch resulting in the formation of a series of cusps each of which remain isolated from one another. At time, t_2, the cusps intersect and coalesce with one another. For a series of uniformly spaced fractures, the time required for intersection (t_2), and thus coalescence, is given by:

$$t_2 = \frac{s}{2r_b} \quad . \tag{12}$$

Before cusp coalescence occurs, i.e. $t < t_2$, the peak-to-valley roughness is defined by the crack depth ($\delta_{PV} = c$). The surface area is also initially large owing to the large number of surface fractures. At t_2, δ_{PV} decreases instantaneously as the cracks are assumed to have vertical sides in

the present model. The surface area also decreases significantly. After coalescence, i.e. $t \geq t_2$, the surface roughness becomes independent of crack depth and scales as:

$$\delta_{PV} = r_b\, t - \sqrt{(r_b\, t)^2 - \tfrac{1}{4}s^2} + \delta_o \qquad (13)$$

where δ_o is the baseline roughness.

One can compare the time evolution of the peak-to-valley (P-V) roughness of ground surfaces generated experimentally with predictions generated using the present simplified geometric model. Such a comparison is shown in Fig. 16. Specifically, Fig. 16a compares the time evolution of the P-V surface roughness, in the spatial range of 0.05-0.25 μm^{-1} (~4-20 μm scale lengths), of the sample which was ground using a 150 grit fixed abrasive with predictions which were generated using the present model. A similar comparison for the sample ground using a 30 μm loose abrasive is shown in Fig. 16b.

The modeled results, in each case, were generated by substituting the average crack spacing and maximum subsurface damage depths that were determined experimentally (see Section 2.2) into Eq. 12 which was used to estimate the initial coalescence time, and Eq. 13 which was used to estimate the time dependent evolution of the P-V roughness. As shown in Table 1, the average crack spacings (s) of the 150 grit fixed abrasive and the 30 μm loose abrasive ground surfaces were found to be 22 μm and 17 μm, respectively. The maximum SSD depths (c) as determined using the taper polish technique [5-7] were 42 μm and 41 μm, respectively (see Table 1). In each case, a bulk etch rate of 1.6 μm/hour, corresponding to that of 20:1 BOE, was used in calculating the model results.

As shown in Figs. 16a and 16b, the model predicts a crack intersection time (see Eq. 12) of 6.9 hours for the 150 grit fixed abrasive ground surface and 5.3 hours for the 30 μm loose abrasive ground surface. For the experimental data, the initial rise in the measured roughness is

an artifact due to the finite (~10 μm) width of the profilometer stylus. A probe of such dimension is incapable of penetrating the narrow, high aspect ratio (~1 μm × 40 μm) cracks present prior to etching. For full penetration, the cracks would have to be etched to a width exceeding ~10 μm. This would require almost four hours of etching (4 hrs × 1.6 μm/hr × 2 ~13 μm) and for a uniform distribution of cracks, would correspond to the maximum P-V roughness. Moreover, if the probe was sufficiently narrow to penetrate all cracks, the initial P-V roughness would equal the subsurface damage (SSD) depth, or ~40 μm, as described by the model. Because of the physical limitations of the profilometer stylus, the true P-V roughness cannot be measured at the onset of etching until the openings of the etched cracks exceed the width of the profilometer stylus. None-the-less, one finds that there is generally good agreement between the experimental data and the modeled results. For example, once the time required to etch beyond the physical dimensions of the profilometer probe is exceeded, the present 2-D geometric model provides a reasonable prediction of the time dependent evolution of the surface roughness.

The present model can also be used to describe the material removal rate as the surface area exposed to the etchant evolves with time. The effective removal rate before the coalescence of adjacent surface fractures ($t < t_2$) is given by the bulk etch rate multiplied by the ratio of the surface area at time t, to the initial flat surface area:

$$\frac{dz_g}{dt} = \frac{r_b}{2s}\left[(2\pi - 8)\, r_b t + 4c + 2s\right] \tag{14}$$

After coalescence ($t \geq t_2$) the removal rate is given:

$$\frac{dz_g}{dt} = \frac{2r_b^2 t}{s} \sin^{-1}\left(\frac{s}{2r_b t}\right) \tag{15}$$

As shown in Figs. 16c and 16d, there is qualitative agreement between the model and the experimental material removal rates. As one would expect, the material removal rate is maximized at the onset of the etching process when the surface area exposed to the etchant is also at a maximum owing to the large number of fracture surfaces. After the cusps begin to coalesce with one another, the surface area decreases and consequently, the removal rate decreases until it converges to the etch rate of the bulk material (r_b). The shortcoming of the present model is also evident in Figs. 16c and 16d. Specifically, whereas the mass removal rate during the etching of each of the ground samples decreases exponentially, the modeled results experience a precipitous drop at a single fracture coalescence time (t_2). This difference is due to the distribution of crack depths and spacings which exists on each of the real ground surfaces [5, 7] rather than the single values of depth (c) and spacing (s) which have been assumed in the present model.

The present results, together with the results discussed in Section 4.2.2, provide an illustration of the utility of etching ground surfaces during the fabrication of SSD free substrates. As shown in Fig. 14, after extended etching, a P-V roughness of ~30 μm is achieved for the 150 grit fixed abrasive ground sample while a P-V roughness of ~20 μm is achieved for the 30 μm loose abrasive ground surface. Recall that the maximum subsurface damage was similar (~42 μm) for each of these samples. By etching the substrate immediately after grinding, one can significantly reduce the amount of material that must be polished away to achieve a SSD-free substrate. The effectiveness of etching in reducing SSD, and thus reducing polishing time, is promoted by grinding processes which yield a high density of fractures that have relatively uniform dimensions, which can readily coalesce with one another during the etching process.

4.3 Finite Difference Etch Model

The etch model discussed in the previous section assumes that each of the fractures are of uniform dimensions and are equally spaced. In the present section, we consider a three dimensional (3D) finite difference model that describes the etching behavior of a surface which contains a distribution of cracks which vary with respect to length, depth, orientation and spacing.

In this model, the initial surface is represented as a height on a two dimensional rectangular grid. This surface is determined statistically from the relevant crack distributions to set positions, crack length and depth. Since only a finite area can be modeled, the resulting surface can be considered as one member of an ensemble of surface patches corresponding to the crack distributions. At a given time, each surface point is assumed to etch along the surface normal. In practice, the surface is represented by the pyramid whose vertices are the heights at a specified grid location plus its four nearest neighbors. The etch direction is then taken as the average of the normals to the four sides of the pyramid. A more detailed quantitative description of the 3D finite difference etch model, as well as its features, are provided in the Appendix. The three-dimensional (3D) finite difference etch model was first evaluated by comparing the coalescence data shown for cracks etching in a scratch (Fig. 4) to values calculated from the model. Figure 17a shows a comparison of the etch model and experimental data for that of a single peak, and illustrates that the convex surface has some enhancement in removal. The mechanism for this enhancement is not currently understood; however, the model has been mathematically calibrated to the experimental data using an enhancement in the etch rate (see Appendix for details). Figure 17b shows the resulting etch simulation with this enhancement and illustrates the improved agreement between the model and the experiment.

The 3D etch model was then used to explore the effect that crack distributions have on the evolution of surface topology during etching. Three scenarios were simulated: 1) randomly spaced and oriented cracks of the same length and depth, 2) ordered cracks of the same length and depth, and 3) randomly spaced and oriented cracks of different lengths and different depths. In each case, the same number of cracks was evaluated using the same grid size. The results of this simulation are shown in Fig. 18 where the top (planar) view of these distributions and the contour maps of these crack distributions, before and after etching for 16 hours, are presented.

As shown by the first scenario, the etch model reveals that in areas where the cracks are spaced far apart, crack intersection and coalescence do not take place and the surface remains high and fairly flat. In such areas, the P-V roughness also changes less than in areas of high crack density. In the areas where the cracks are spaced closer together, the cracks are able to intersect and coalesce with one another leading to a reduction in surface roughness. As shown by the second scenario, the reduction in P-V roughness is most efficient when the majority of the cracks are closely spaced. This reinforces the idea that etching most efficiently converts SSD to surface roughness for surfaces which are characterized by a uniform distribution of closely spaced cracks. However, because real ground surfaces typically consist of a distribution of crack lengths, depths, orientations, and spacings, a third scenario was evaluated by the 3-D etch code. The roughness and mass removal rates as a function of etch time for each of the three simulations are compared in Fig. 19. These results are qualitatively similar to those found experimentally using the 2D code; both the roughness and the removal rate were initially high but decreased with etch time. The rate of surface fracture transformation to roughness is strongly governed by the crack number density and the spatial distribution of cracks.

5. CONCLUSIONS

The effects of HF/NH_4F (BOE) wet chemical etching on the morphology of isolated surface defects (indentations and scratches) and of ground surfaces have been characterized for fused silica glass. For polished surfaces, fluoride etching has proven to be a simple and significant aid in assessing the presence of surface defects (scratches and digs) during the fabrication process. Moreover, etching has proven to be helpful in revealing the true size and morphology of fractures which might otherwise be obscured by the presence of the Bielby layer, and the fractures which are of an insufficient size to reflect or scatter light. Three types of indentation fractures have been examined: blunt indentations (Hertzian cracks), sharp (Vickers) indentations (radial and lateral cracks), and scratches (trailing indentation cracks). The crack morphologies observed were consistent to those that had previously been reported elsewhere. Similarly, there was also good agreement between the measured crack dimensions and those which are calculated from standard fracture indentation relationships.

When isolated fractures are etched, the bottom and the sides of the fractures etch at nominally the same rate, making the removal of such defects by etching impractical. In contrast, when ground surfaces are etched, as each of the individual cracks open laterally, they may intersect and coalesce with numerous adjacent cracks. This behavior results in the formation of a cusp-like morphology whose diameter increases with the square root of etch time. Particularly in cases where there is a uniform distribution of closely spaced cracks, this phenomenon can be used to reduce both the extent of SSD and surface roughness. Similarly, the rate of etching for a ground surface is always elevated relative to the bulk due to the large surface area presented by the numerous fracture surfaces. As etching proceeds, the material removal (etch) rate decreases as the surface area associated with fracture surfaces is reduced, until the bulk etch rate is reached.

For ground surfaces, etching provides a means of reducing or eliminating the SSD introduced by the grinding process. This provides an economical way of reducing the amount of material that must be removed by subsequent grinding or polishing processes in order to yield SSD-free surfaces. Etching also ensures that most, if not all, of the SSD has been effectively removed prior to the next processing step as SSD can be readily seen as cusps after etching. Simple, geometric and isotropic etch models that predict the material removal and surface evolution of ground fused silica surfaces have been developed and can be used as guidelines to optimize the optical fabrication process.

ACKNOWLEDGEMENTS

The authors would like to thank James Embree for his assistance in performing the grinding processes on the samples. Work performed under the auspices of the U. S. Department of Energy by Lawrence Livermore National Laboratory under Contract No. DE-AC52-07NA27344, with the LDRD program.

Appendix: Finite Difference Etch Model

This appendix describes a finite difference model of the isotropic etching of a surface. At time t_0, the surface is represented by an array of points in Cartesian coordinates (x,y,S) in which the z component $S(x,y,t_o)$ is the height of the surface at position x,y. The values of x,y are uniformly spaced (δx and δy) in the base plane using an array index of i_o, j_o where $x = i_o\delta_x$ and $y = j_o\delta_y$. The basic idea is that the surface etches along the local surface normal. Numerically, the surface at time $t_o+\Delta t$ is determined by moving each surface point along the direction which is the average normal of the surface facets surrounding the given point (see Fig. 20). This vector displacement $\vec{d}_T(x,y)$ of the point (x,y,S) is defined as:

$$\vec{d}_T(x,y) = r_b\ \Delta t\ \hat{n}(x,y) \tag{A1}$$

where r_b is the base etch rate (thickness/time) and $\hat{n}(x,y)$ is the unit vector defined by the average of the normal unit vectors of each of the nearest neighbor planes containing the given point. This average normal unit vector is given by:

$$\hat{n}(x,y) = (n_x(x,y), n_y(x,y), n_z(x,y)) = \frac{\hat{n}_1 + \hat{n}_2 + \hat{n}_3 + \hat{n}_4}{\left|\hat{n}_1 + \hat{n}_2 + \hat{n}_3 + \hat{n}_4\right|} \tag{A2}$$

where n_x, n_y and n_z are the components of the average normal vector and where

$$\hat{n}_1 = \frac{\overrightarrow{AC}\times\overrightarrow{AB}}{\left|\overrightarrow{AC}\times\overrightarrow{AB}\right|} \quad \hat{n}_2 = \frac{\overrightarrow{AE}\times\overrightarrow{AB}}{\left|\overrightarrow{AE}\times\overrightarrow{AB}\right|} \quad \hat{n}_3 = \frac{\overrightarrow{AD}\times\overrightarrow{AE}}{\left|\overrightarrow{AD}\times\overrightarrow{AE}\right|} \quad \hat{n}_4 = \frac{\overrightarrow{AC}\times\overrightarrow{AD}}{\left|\overrightarrow{AC}\times\overrightarrow{AD}\right|} \tag{A3}$$

Here $\overrightarrow{AB}$, $\overrightarrow{AC}$, $\overrightarrow{AD}$, and $\overrightarrow{AE}$ are the vectors described by the points **A**-**E** (see Fig. 20). The numerical subscripts represent the four planar facets connecting Point **A** with its nearest neighbors. The new surface is then calculated for every original point (i_o,j_o) on the surface using Eq. A1-A3 for a time increment Δt using:

$$
\begin{aligned}
i &= i_o - r_b \Delta t \, n_x \\
j &= j_o - r_b \Delta t \, n_y \\
S(i, j, t_o + \Delta t) &= S(i_o, j_o, t_o) - r_b \Delta t \, n_z
\end{aligned}
\tag{A4}
$$

After time increment Δt, the basal points corresponding to the heights $S(x,y,t_o+\Delta t)$ are most likely not uniformly spaced by δx and δy. For ease of continuing the surface calculation for many time increments, it is convenient to interpolate the surface array $S(x,y, t_o+\Delta t)$ back to the original uniform grid of x,y points. To illustrate this process, consider the x,y projection of point **a** and its nearest neighbors (points **b-e**) at time $t+\Delta t$ onto original point **A** and its nearest neighbors (points **B-E**). To interpolate back to the original x, y grid, we want to calculate the equivalent depth z_e for point **a** at point **A** (see Fig 21). This can be done by first determining which of the nearest neighbor planes point **A** resides in, which is determined by the minimum average distance to any of the nearest neighbor points. The desired value can then be found by interpolation between the three values at the (i,j,S) points that define this plane. For example, as shown in Fig 21, the nearest neighbor plane for Point **A** contains points **a**, **b** and **e**. The normal direction for this plane is along:

$$
\vec{n}_2 = \overrightarrow{ab} \times \overrightarrow{ae} = (n_{2x}, n_{2y}, n_{2z}) \tag{A5}
$$

where n_{2x}, n_{2y} and n_{2z} are the components of the vector. By defining the components of Point **A** as (i_o,j_o) and those of Point **a** as (i,j), the interpolated height corresponding to point **a** at Point **A** is given by :

$$
S(i_o, j_o, t_o + \Delta t) = \frac{-n_{2x}}{n_{2z}}(i_0 - i) - \frac{n_{2y}}{n_{2z}}(j_0 - j) + S(i, j, t_o + \Delta t) \tag{A6}
$$

This interpolation process is repeated for every point after each time increment.

As discussed in Section 4.3 and Fig. 17a, experimentally there is an enhancement in removal on convex surfaces. To account for this effect in our model, the etch rate is enhanced by locally increasing the magnitude of the surface displacement vector to:

$$\vec{d}_T(x,y) = r_b \Delta t \; \hat{n}(x,y)\,(1+Q(x,y)) \tag{A7}$$

where Q(x,y) is the local relative enhancement and depends on the local curvature. Figure 23 shows an x, z projection where Point A is on a convex surface. Note the magnitude of the normal vector is enhanced by a factor of 1+Q. The mechanism of the enhancement is not understood; however, we found good correspondence with the experimental data when Q was empirically defined for a given δ_x, δ_y as:

$$Q(i,j) = 0.4\left(1 - e^{-(4\cdot S(i,j) - S(i+1,j) - S(i-1,j) - S(i,j+1) - S(i,j-1))^2}\right) \tag{A8}$$

where the value in the exponent is related to the curvature about Point A (i,j).

Because the numerical method described above is explicit, unless the time step is very small, it is possible to induce numerical instabilities in which high spatial frequency features grow exponentially fast. One way to avoid these instabilities and allow a more generous time step is to smooth away the highest spatial frequencies. We have chosen to do this by adding a pseudo-diffusion step to the algorithm described above. To see how to implement this, consider the diffusion equation

$$\frac{\partial S}{\partial t} = D_e\left(\frac{\partial^2 S}{\partial x^2} + \frac{\partial^2 S}{\partial y^2}\right) \tag{A9}$$

where D_e is the effective diffusion constant. This equation is easily solved if the surface height S is written as a Fourier transform $\tilde{s}(k_x, k_y)$ where k_x and k_y are the spatial frequencies in the x and y direction. If we take

$$S(x, y, t) = \sum_{k_x, k_y} \tilde{s}(k_x, k_y)\, e^{i(k_x x + k_y y)} \tag{A10}$$

the solution to Eq.(A9) is given by

$$S(x, y, t + \Delta t) = \sum_{k_x, k_y} \tilde{s}(k_x, k_y)\, e^{-D_e\left(k_x^2 + k_y^2\right)\Delta t} e^{i\left(k_x x + k_y y\right)} \tag{A11}$$

In practice, for each time step integration, we first transform to the spectral domain, i.e. Fourier transform the present surface S, thus finding $\tilde{s}(k_x, k_y)$. We then multiply each $\tilde{s}(k_x, k_y)$ by the term $e^{-D_e\left(k_x^2 + k_y^2\right)\Delta t}$ and inverse Fourier transform back to the spatial domain. This accomplishes the smoothing after which we evaluate Eq. (A7) at each point. The exponential term in Eq. (A11) amounts to a low pass filter, i.e. it preferentially filters out high spatial frequencies. The important parameter in this process is $\sqrt{\frac{D_e \Delta t}{\delta x^2}}$ which is the ratio of the smoothing length to the grid size. When this parameter is of order one, the highest spatial frequencies supported by the grid ($k_x^{max} = \frac{\pi}{\delta x}$) are attenuated at each time step while slightly lower frequencies are hardly affected because of the exponential dependence of the filtering function on $k_x^2 + k_y^2$.

REFERENCES

1) G. Spierings, "Review – Wet Chemical Etching of Silicate Glasses in Hydrofluoric Acid Based Solutions," J. Mat. Sci., 28 (1993) 6261-6273.

2) H. Kikyuama, N. Miki, K. Saka, J. Takano, I. Kawanabe, M. Miyashita, T. Ohmi, "Principles of Wet Chemical Processing in ULSI Microfabrication," IEEE Trans. Semiconductor Mfg, 4 (1) (1991) 26-35.

3) F. Preston, "Structure of Abraded Surface Glasses," Trans. Opt. Soc., 23(3) 141-162 (1922).

4) Y. Zhou, P. Funkenbusch, D. Quesnel, D. Golini, and A. Lindquist, "Effect of Etching and Imaging Mode on the Measurement of Subsurface Damage in Microground Optical Glasses," J. Amer. Ceram. Soc. 77 (1994) 3277-3280.

5) T. Suratwala, L. Wong, P. Miller, M. D. Feit, J. Menapace, R. Steele, P. Davis, D. Walmer, "Subsurface Mechanical Damage Distributions During Grinding of Fused Silica," J. Non. Cryst. Solids, 352 (2006) 5601-5617.

6) J. Menapace, P. Davis, L. Wong, W. Steele, T. Suratwala, P. Miller, "Measurement of Process-Dependent Subsurface Damage in Optical Materials Using the MRF Technique," SPIE 5991, Boulder Damage Symposium XXXVII (2005).

7) P. Miller, T. Suratwala, L. Wong, M. Feit, J. Menapace, P. Davis, R. Steele, "The Distribution of Subsurface Damage in Fused Silica," SPIE 8991, Boulder Damage Symposium XXXVII (2005).

8) W. Kline, H. S. Folger, "Dissolution of Silicate Minerals by Hydrofluoric Acid," Ind. Eng. Chem. Fundam., 20 (2) (1981) 155-161.

9) H. Prosksche, G. Nagorsen, "The Influence of NH_4F on the Etch Rate of Undoped SiO_2 in Buffered Oxide Etch," J. Electrochem. Soc., 139 (1992) 521-524.

10) H. Kikyuama, M. Waki, I. Kawanabe, M. Miyashita, T. Yabune, N. Miki, "Etching Rate and Mechanism of Doped Oxide in Buffered Hydrogen Fluoride Solution," J. Electrochem. Soc., 139 (1992) 2239-2243.

11) J. Judge, J. Electrochem. Soc., "A Study of the Dissolution of SiO_2 in Acidic Fluoride Solutions," 118 (11) (1971) 1772-1775.

12) H. Broene, T. DeVries, "The Thermodynamics of Aqueous Hydrofluoric Acid Solutions," J. Amer. Chem. Soc., 69 (1947) 1644-1646.

13) W. Kline, H. S. Fogler, "Dissolution Kinetics: Catalysis by Strong Acids," J. Colloid Interface Sci., 82 (1) (1981) 93-102.

14) C. Iliescu, F. E. H. Tay, "Wet Etching of Glass", Semiconductor Conference, 2005. CAS 2005 Proceedings, 2005 International, Vol. 1, 3-5 October 2005, pages 35-44.

15) A. Witvrouw, B. DuBois, P. DeMoor, A. Verbist, C. VanHoof, H. Bender, K. Baert, "A Comparison Between Wet HF Etching and Vapor HF Etching for Sacrificial Oxide Removal," SPIE 4174, Micromaching and Microfabrication Process Technology VI (2000) 130-141.

16) M. D. Feit, A. M. Rubenchik, "Influence of Subsurface Cracks on Laser Induced Surface Damage," SPIE 5273 (2003) 264-272.

17) B. Lawn, "Fracture of Brittle Solids - Second Edition", Cambridge Solid State Science Series (1993)

18) F. C. Roesler, "Brittle Fractures Near Equilibrium," Proc. Phys. Soc. Lond., B69 (1956) 981-992.

19) J. T. Hagan, "Cone Cracks Around Vickers Indentations in Fused Silica Glass," J. Mat. Sci., 14 (1979) 462-466.

20) I. M. Hutchings, "Tribology: Friction and Wear of Engineering Materials," Edward Arnold, UK (co-published by CRC Press) (1992).

21) G. Bielby, Aggregation and Flow of Solids, 1st Ed, London: Macmillan and Co. (1921).

22) D. E. Gray, American Institute of Physics Handbook, 3rd Edition, McGraw Hill, New York (1973).

23) S. M. Wiederhorn and P. R. Townsend, "Crack Healing in Glass," J. Am. Ceram. Soc., 53 (1970) 486-489.

24) W. D. Kingery, H. K. Bowen, D. R. Uhlmann, "Introduction to Ceramics – Second Edition", John Wiley & Sons, New York (1960).

List of Tables

List of Figures

Figure 6. Measured cusp diameter vs. etch time$^{1/2}$ for the ground fused silica surfaces etched in 20:1 BOE.

Figure 7. The subsurface damage (SSD) depth distributions for the 150 grit fixed abrasive ground and 30 μm loose abrasive ground samples.

Figure 8. (Top) Edge or side-lit images of a polished fused silica surface, before and after etching. (Bottom) Schematic showing the cross-section of the glass surface containing hidden cracks prior to etching which open up after etching.

Figure 9. Schematic cross-sectional view of (a) Hertzian indent, (b) Vickers indent, and (c) sliding indent, before and after etching.

Figure 10. Schematic illustration of the opening of Hertzian cone cracks with etching; the solid lines represent surfaces before etching and the dashed lines represent surfaces after etching for time, t.

Figure 11. (a) Comparison of the measured crack widths of the Hertzian cracks (w_h) from Brinnell indentation on the fused silica surface after etching to that predicted by Eq. 6. (b) Comparison of half of the measured radial crack width (w_r) to the amount of the base thickness removed as a function of etch time.

Figure 12. Mass and thickness removal rate as a function of etch time for the ground fused silica surfaces.

Figure 13. Power Spectral Density (PSD) for roughness for the (a) 150 grit fixed abrasive ground surface and (b) 30 μm loose abrasive ground surface, as a function of etch time.

Figure 14. Peak-to-Valley (top) and RMS (bottom) roughness for the (a) 150 grit fixed abrasive ground surface and (b) 30 μm loose abrasive ground surface, for different spatial ranges.

Figure 15. Simple, 2-D, geometric model describing the evolution of the surface profile of cracks with etch time.

Figure 16. Comparison of the experimental roughness (top) and mass removal rate (bottom) to the 2-D etch model (Eqs. 13-15) for the (a) 150 grit fixed abrasive ground surface and (b) 30 μm loose abrasive ground surface.

Figure 17. Comparison of the 3-D Etch Model profile results (dotted lines) to the experimental results (solid lines) for a single convex surface of a trailing indent crack (a) without enhancement at the peak and (b) with enhancement at the peak (given by Eqs. A7 & A8).

Figure 18. The 3-D, finite difference etch model simulation results for three different distributions of cracks on the surface.

Figure 19. The 3-D, finite difference etch model results for (a) surface roughness and (b) mass removal rate, as a function of etch time, for three different distributions of cracks on the surface.

Figure 20. x-y projection of Point **A** on surface S and its nearest neighbors points **B**, **C**, **D** and **E** at t_o. The dashed lines outline the four different planes (1,2,3 & 4) that can be described containing Point **A**.

Figure 21. x-y projection of Point **A** on surface S and its nearest neighbors points **B**, **C**, **D** and **E** at time zero and time Δt (shown by equivalent point with lower case letters).

Figure 22. x, z projection of points **A**, **C**, & **E** at t_o and points **a**, **c**, and **e** at $t_o+\Delta t$

Table 1:

Indentation parameters	Variable	150 grit Fine Blanchard	30 μm Loose Abrasive
SSD Depth, (μm)*	c	42	41
Maximum Crack Length (μm)*	L_{max}	94	134
Average Crack Length (μm)*	<L>	15	14
Average Crack Width (μm)*	w	4.4	4.4
Average Crack Spacing (μm)	s	22	17
Pre-exponent for Crack Distribution*	A	1.01	0.96
Annihilation Time (hrs)	t_2	8	6
Measured P-V Roughness after Stabilization (μm)	δ_{PV}	30	20

* data from ref [7]

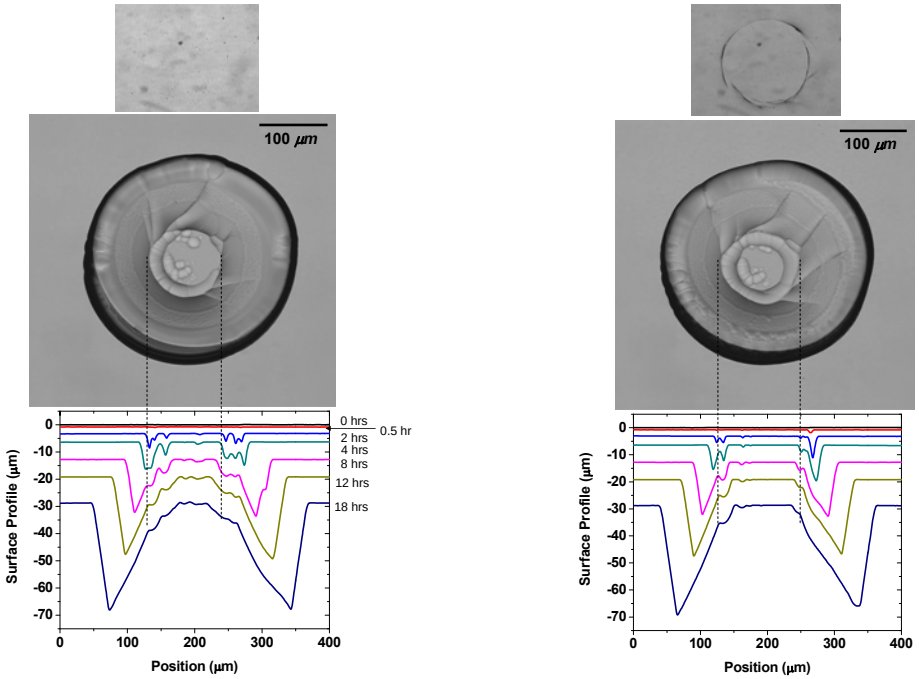
100 μm
Surface Profile (μm)
Position (μm)
0 hrs
0.5 hr
2 hrs
4 hrs
8 hrs
12 hrs
18 hrs
(a)
(b)
(c)
(d)

Figure 1.

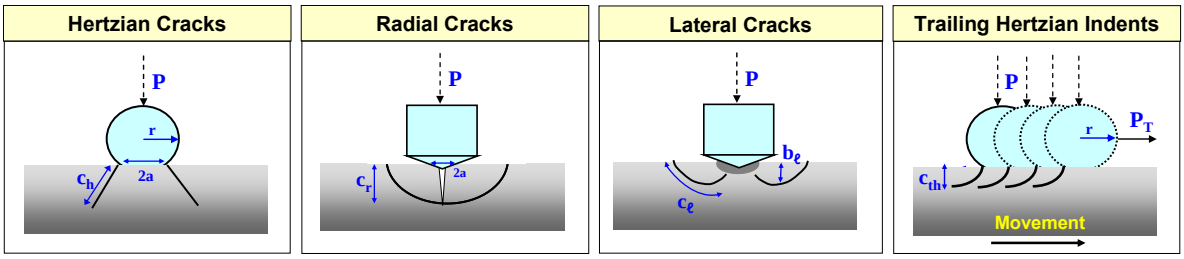

(a) (b) (c) (d)

Figure 2.

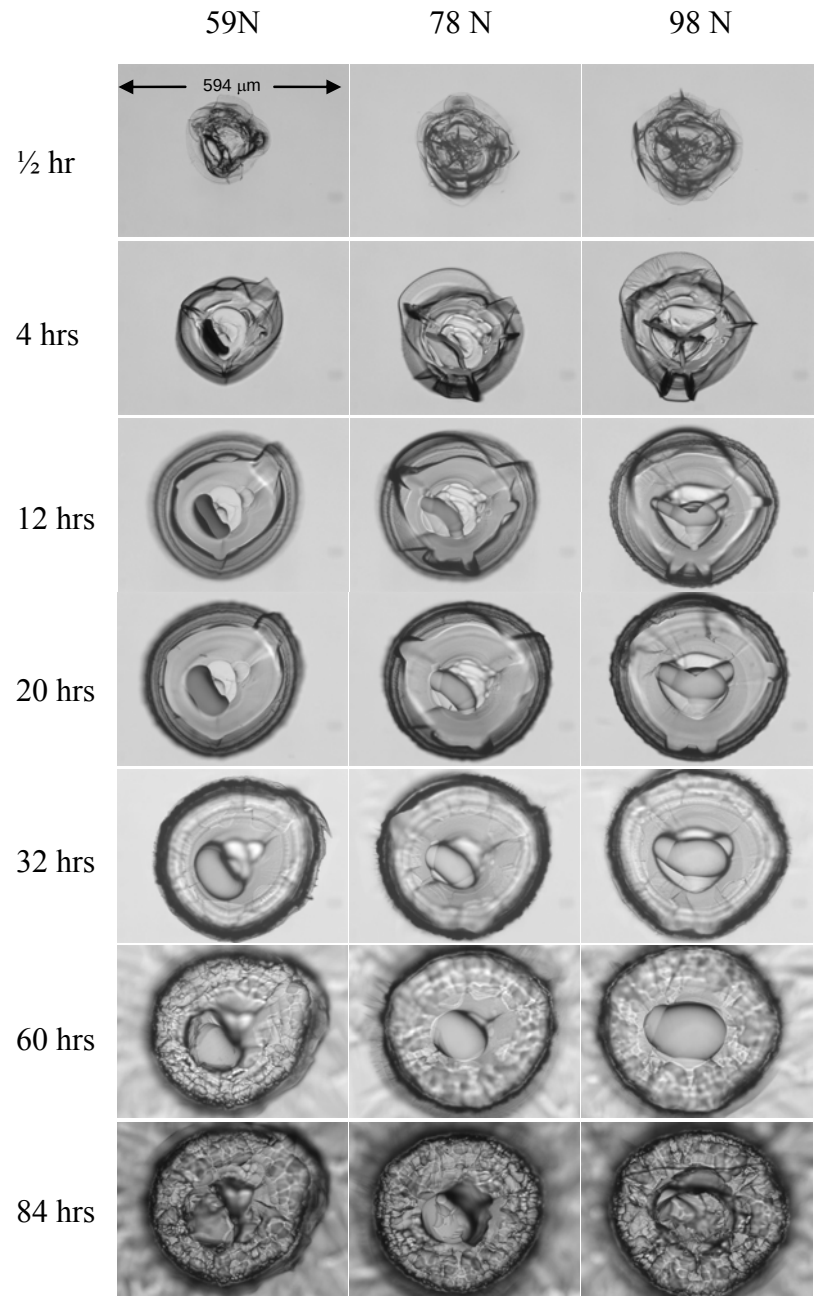

Figure 3.

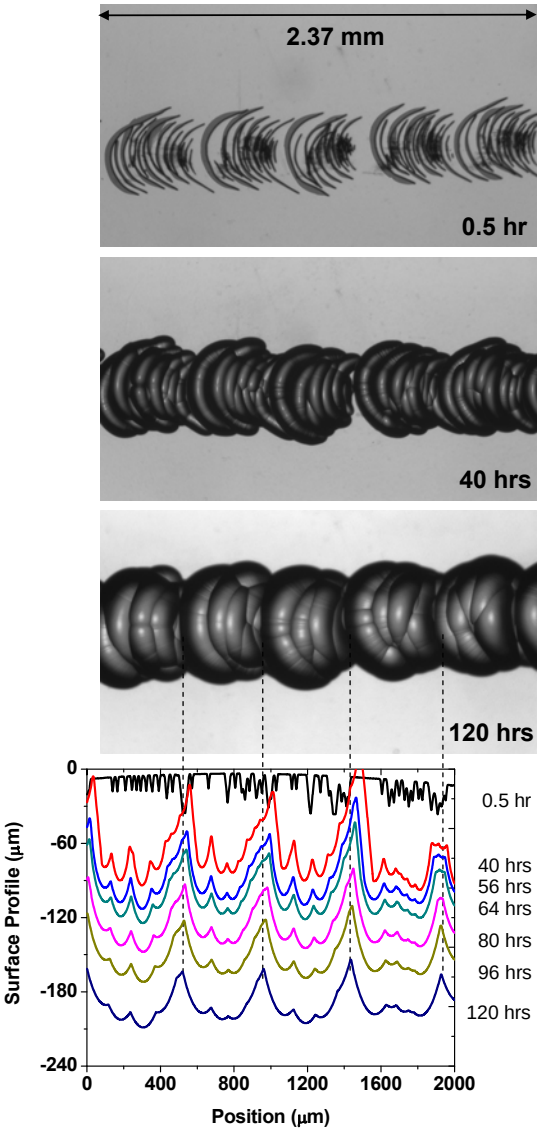
2.37 mm
0.5 hr
40 hrs
120 hrs
Surface Profile (μm)
Position (μm)
0
-60
-120
-180
-240
0
400
800
1200
1600
2000
0.5 hr
40 hrs
56 hrs
64 hrs
80 hrs
96 hrs
120 hrs

Figure 4.

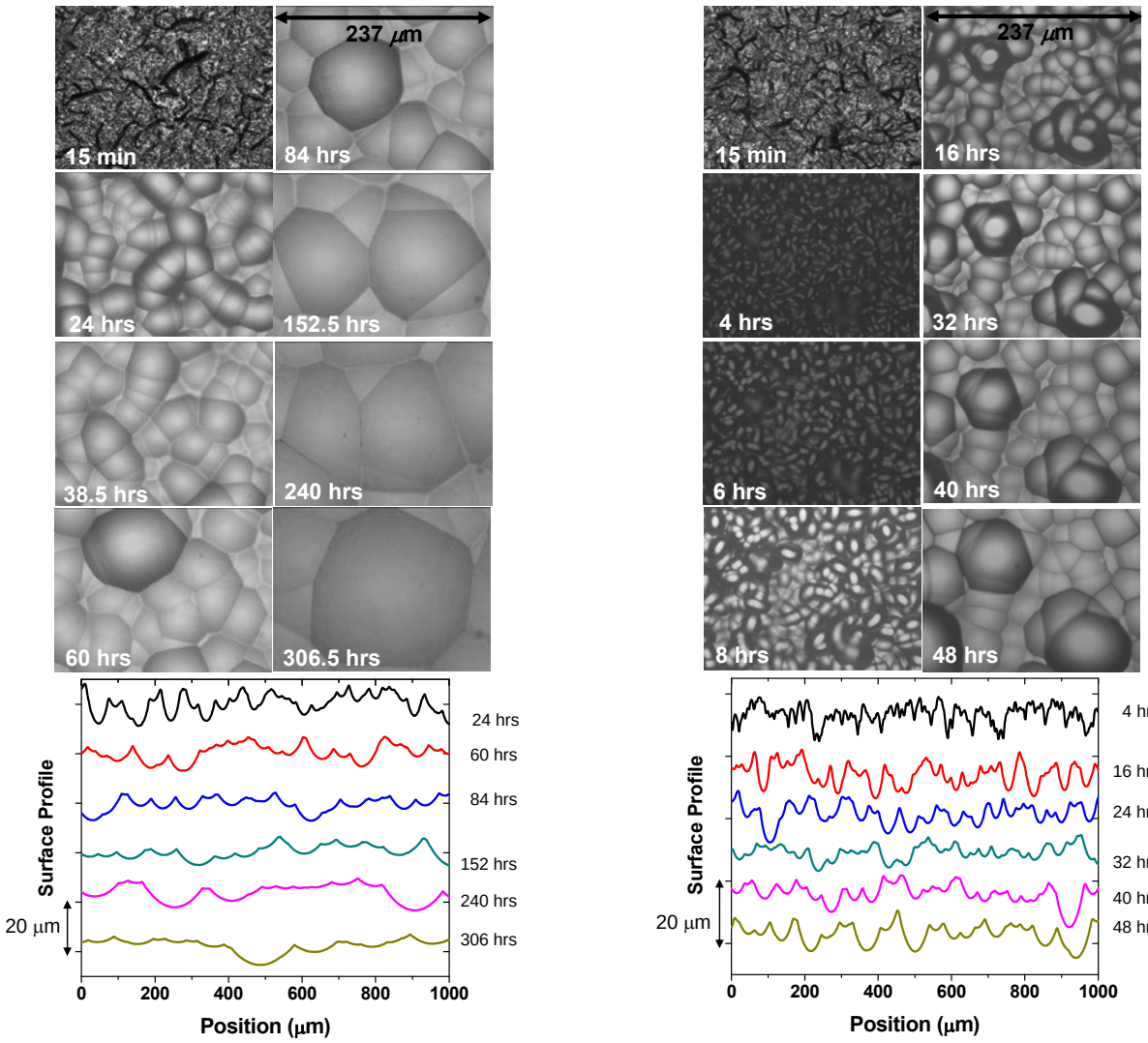
237 μm
15 min
84 hrs
24 hrs
152.5 hrs
38.5 hrs
240 hrs
60 hrs
306.5 hrs
Surface Profile
20 μm
24 hrs
60 hrs
84 hrs
152 hrs
240 hrs
306 hrs
0
200
400
600
800
1000
Position (μm)
237 μm
15 min
16 hrs
4 hrs
32 hrs
6 hrs
40 hrs
8 hrs
48 hrs
Surface Profile
20 μm
4 hrs
16 hrs
24 hrs
32 hrs
40 hrs
48 hrs
0
200
400
600
800
1000
Position (μm)

(a) (b)

Figure 5.

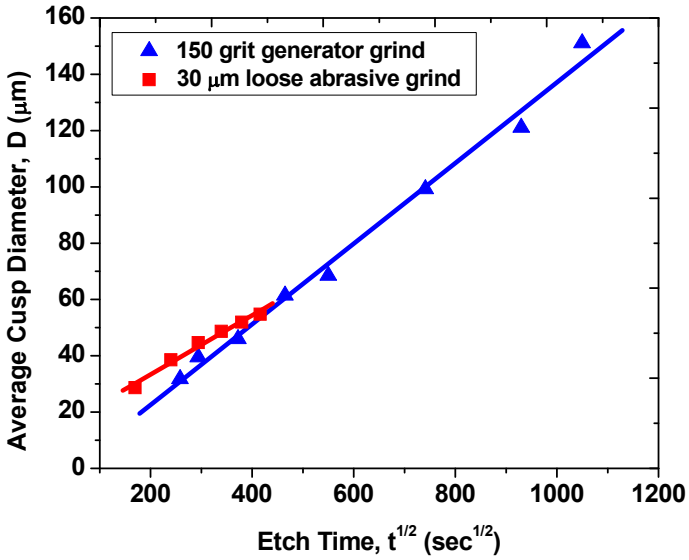

Figure 6.

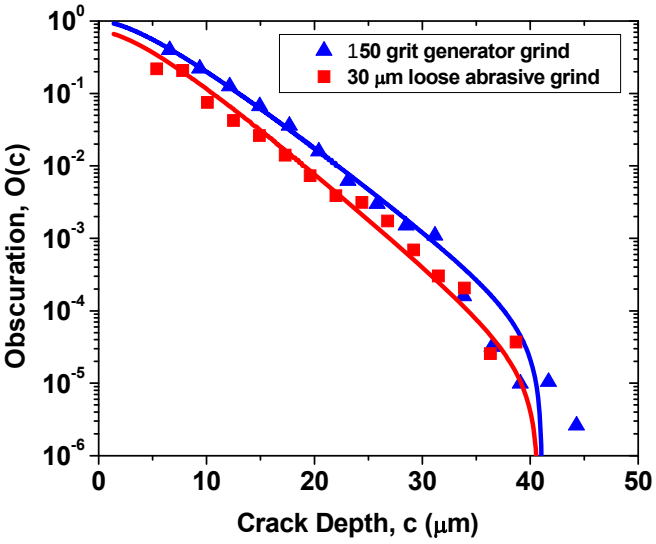

Figure 7.

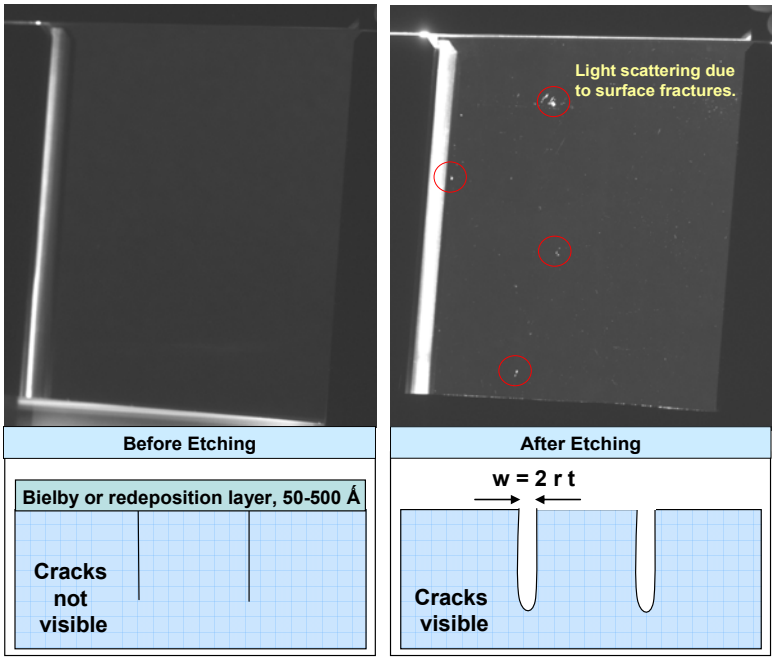
Light scattering due
to surface fractures.
Before Etching
After Etching
Bielby or redeposition layer, 50-500 Á
Cracks
not
visible
w = 2 r t
Cracks
visible

(a) (b)

Figure 8.

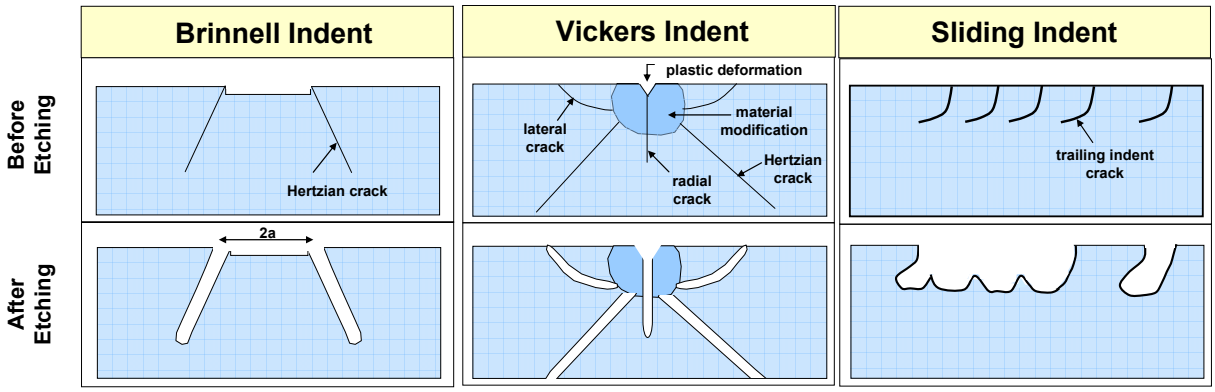

(a) (b) (c)

Figure 9.

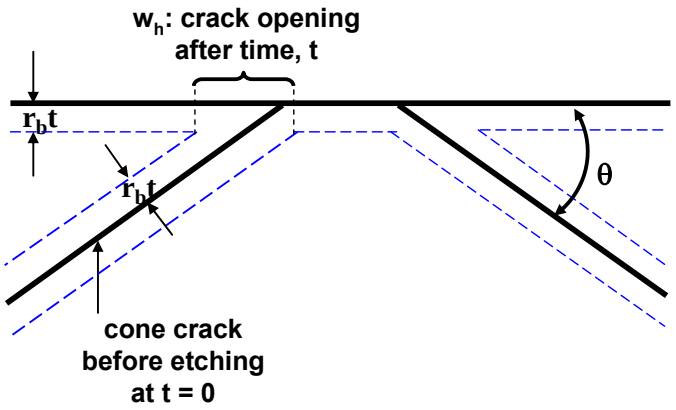

Figure 10.

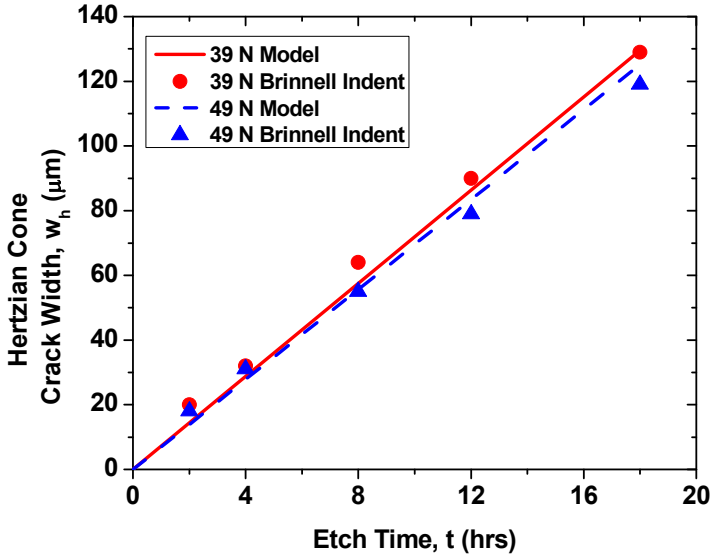
39 N Model
39 N Brinnell Indent
49 N Model
49 N Brinnell Indent
Hertzian Cone
Crack Width, w_h (μm)
Etch Time, t (hrs)
0
20
40
60
80
100
120
140
0
4
8
12
16
20

(a)

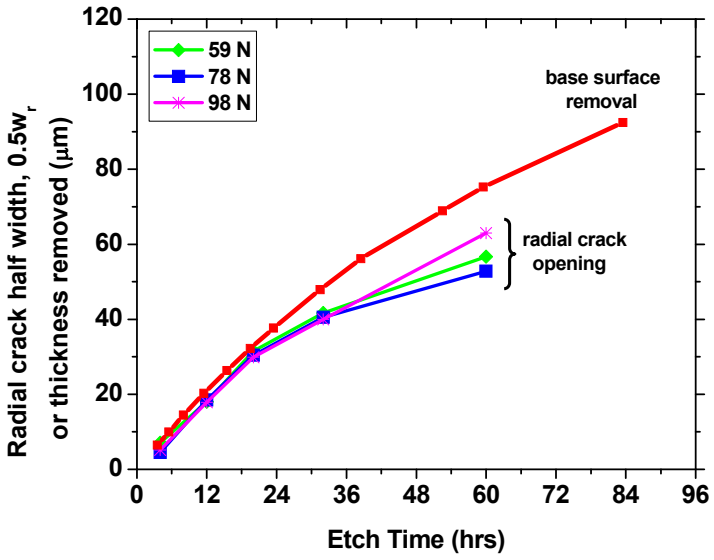
59 N
78 N
98 N
base surface
removal
radial crack
opening
Radial crack half width, 0.5w_r
or thickness removed (μm)
Etch Time (hrs)
0
20
40
60
80
100
120
0
12
24
36
48
60
72
84
96

(b)

Figure 11.

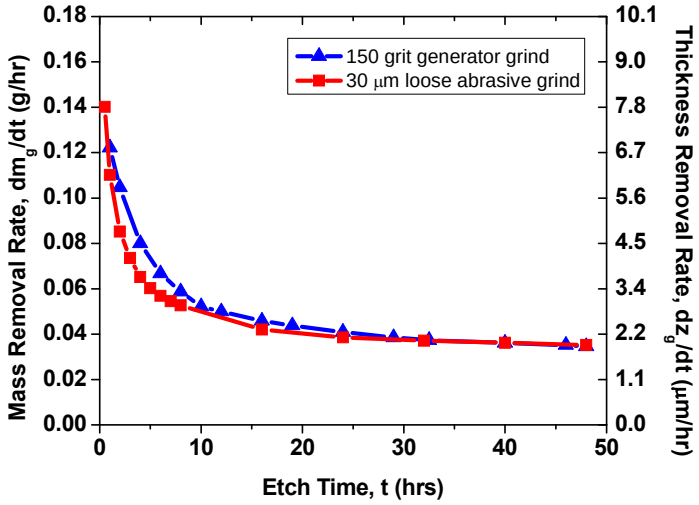

Figure 12.

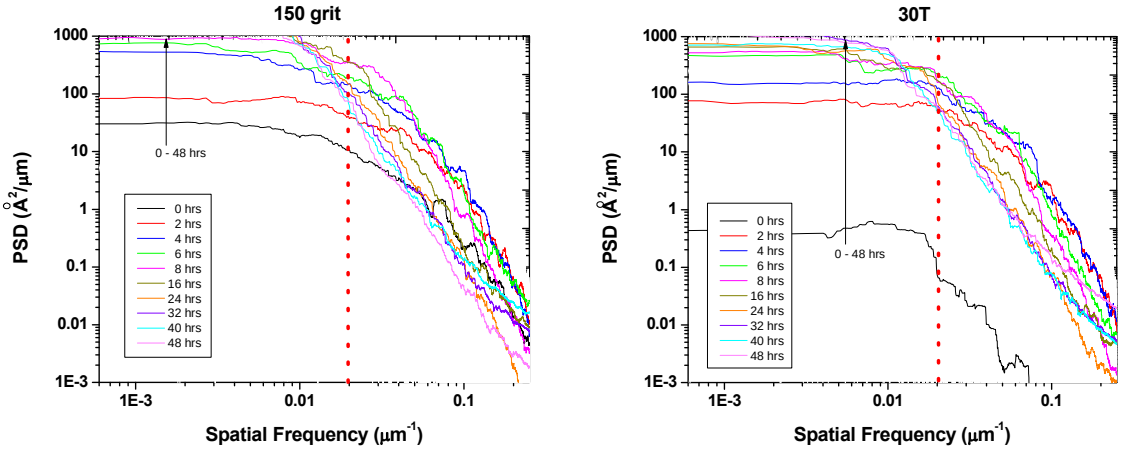

(a) (b)

Figure 13.

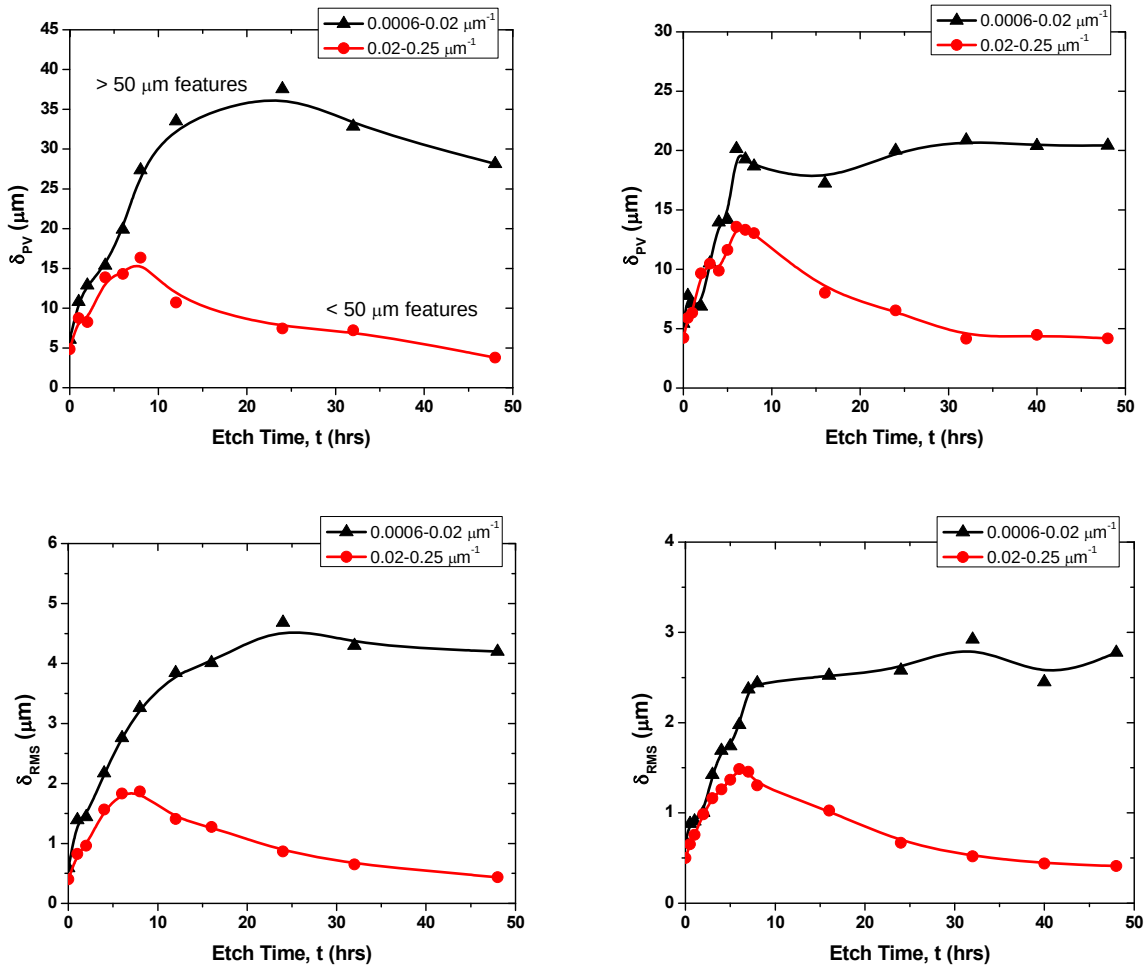
0.0006-0.02 μm-1
0.02-0.25 μm-1
> 50 μm features
< 50 μm features
δPV (μm)
δRMS (μm)
Etch Time, t (hrs)

(a) (b)

Figure 14.

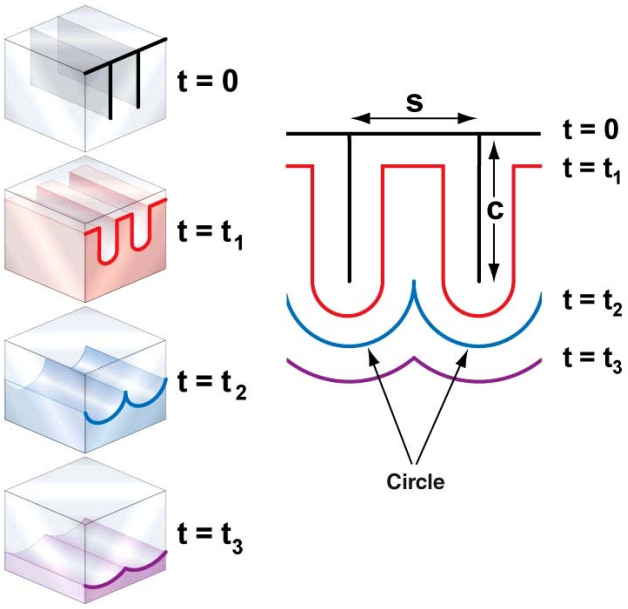

Figure 15.

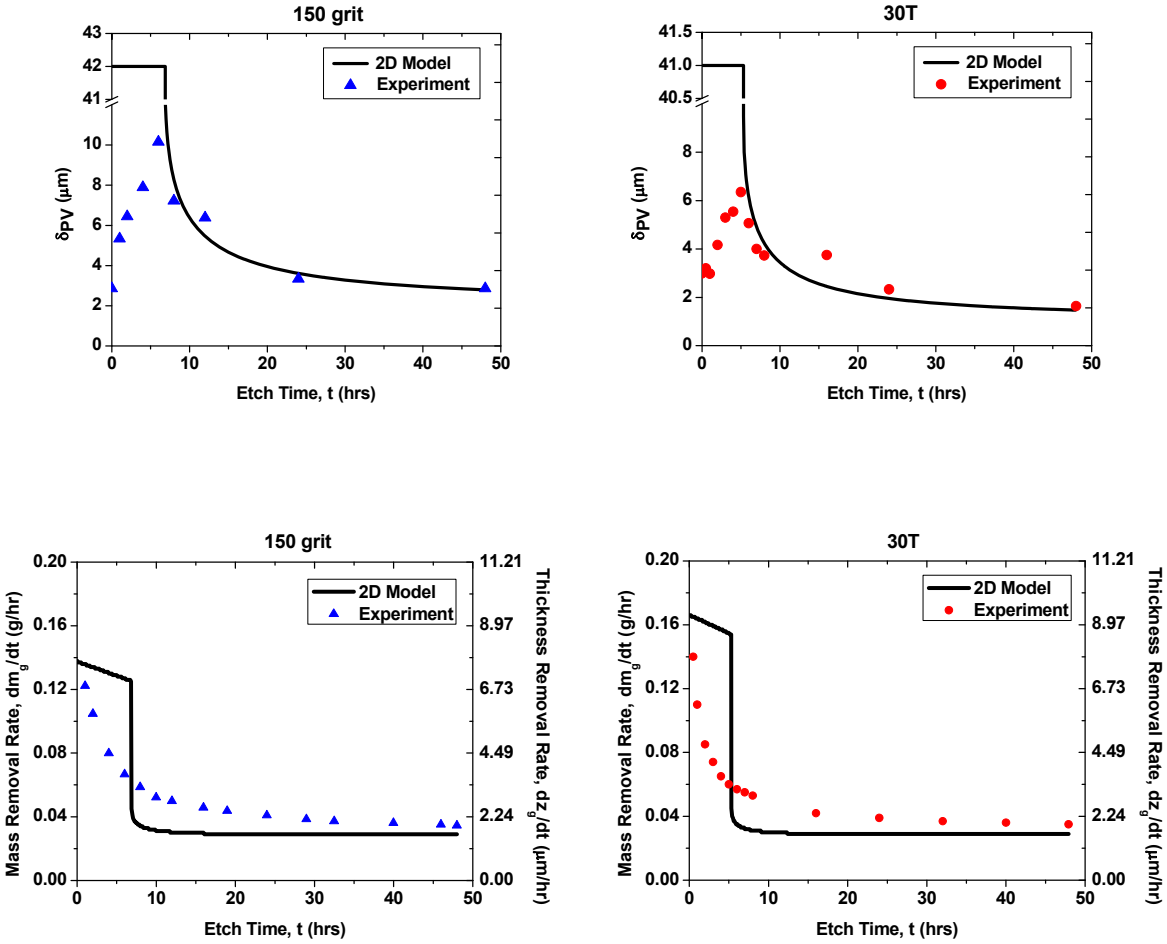
150 grit
2D Model
Experiment
δpv (μm)
Etch Time, t (hrs)
30T
2D Model
Experiment
δpv (μm)
Etch Time, t (hrs)
150 grit
2D Model
Experiment
Mass Removal Rate, dm_g/dt (g/hr)
Thickness Removal Rate, dz_g/dt (μm/hr)
Etch Time, t (hrs)
30T
2D Model
Experiment
Mass Removal Rate, dm_g/dt (g/hr)
Thickness Removal Rate, dz_g/dt (μm/hr)
Etch Time, t (hrs)

(a) (b)

Figure 16.

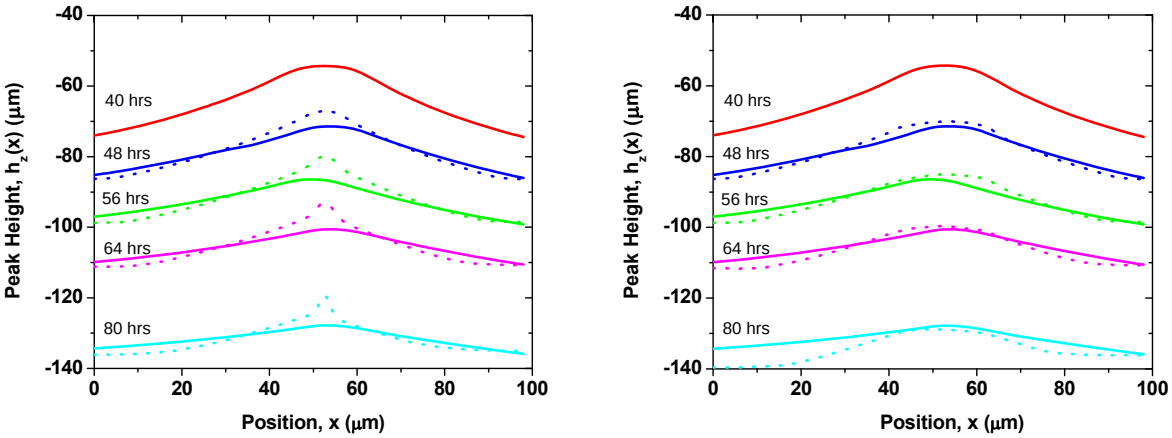
-40
-60
-80
-100
-120
-140
0
20
40
60
80
100
Peak Height, h2(x) (μm)
Position, x (μm)
40 hrs
48 hrs
56 hrs
64 hrs
80 hrs

(a) (b)

Figure 17.

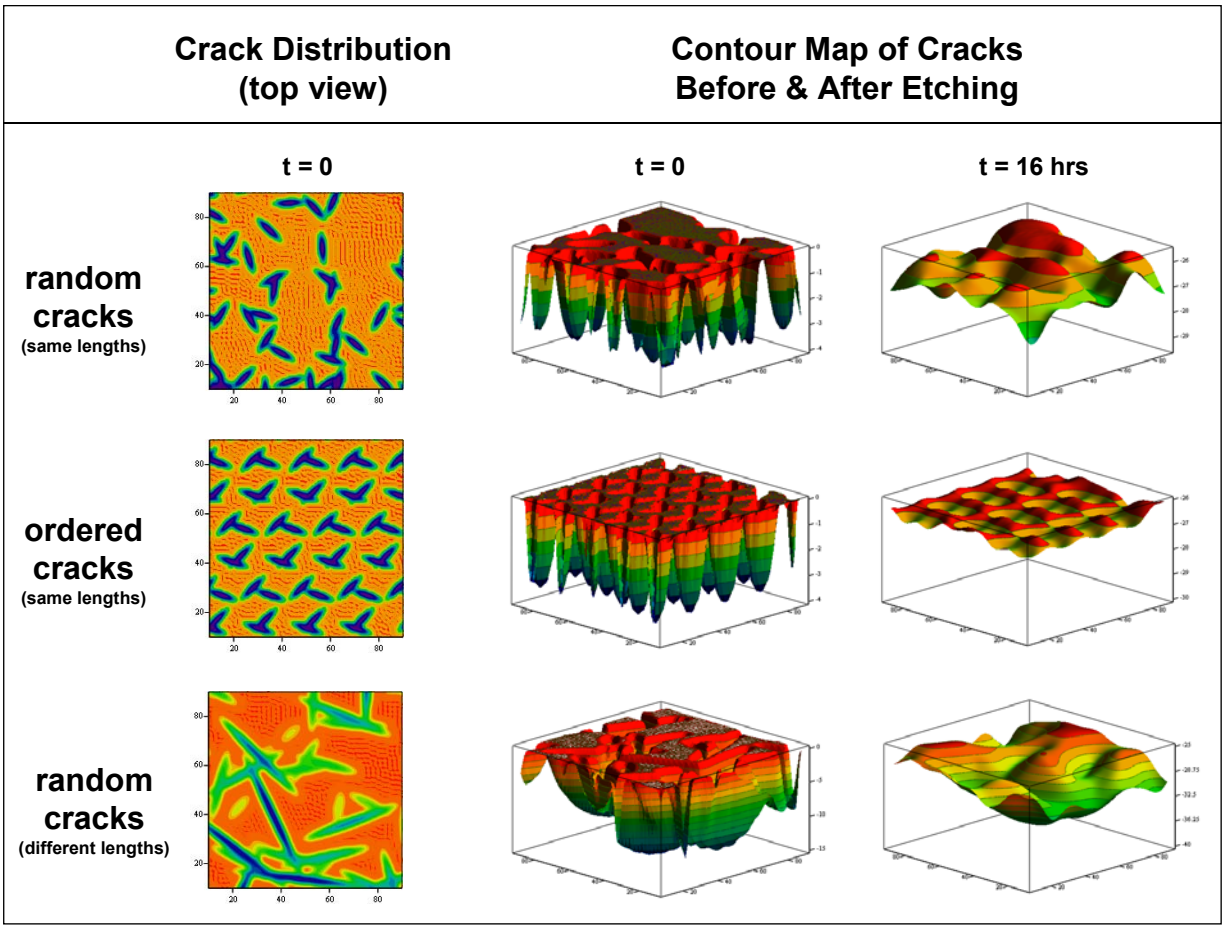
Crack Distribution
(top view)
Contour Map of Cracks
Before & After Etching
t = 0
t = 0
t = 16 hrs
random
cracks
(same lengths)
ordered
cracks
(same lengths)
random
cracks
(different lengths)

Figure 18.

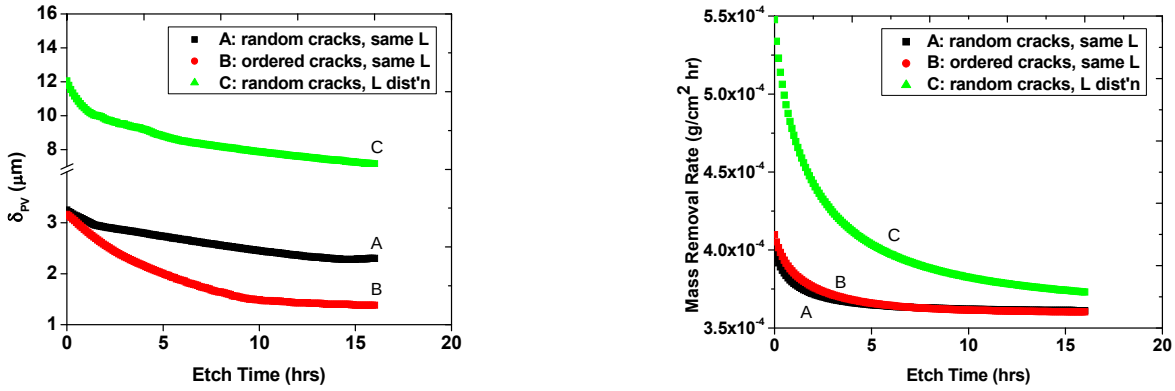

(a) (b)

Figure 19.

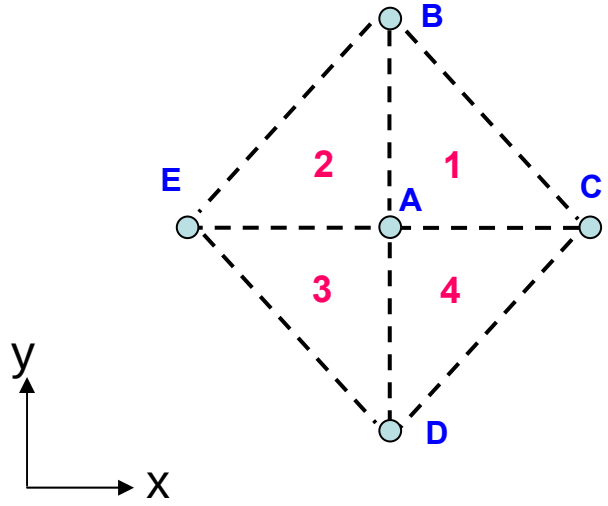

Figure 20.

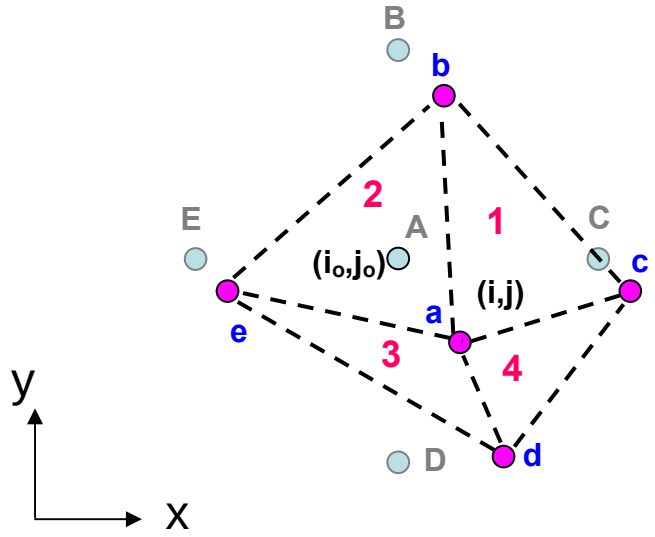

Figure 21.

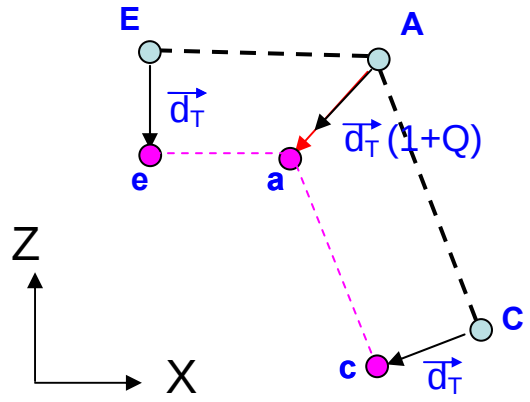

Figure 22.